

Methods to Calculate Electronic Excited-State Dynamics for Molecules on Large Metal Clusters with Many States: Ensuring Fast Overlap Calculations and a Robust Choice of Phase

Hsing-Ta Chen,* Junhan Chen, D. Vale Cofer-Shabica, Zeyu Zhou, Vishikh Athavale, Gregory Medders, Maximilian F. S. J. Menger, Joseph E. Subotnik, and Zuxin Jin



Cite This: *J. Chem. Theory Comput.* 2022, 18, 3296–3307



Read Online

ACCESS |



Metrics & More

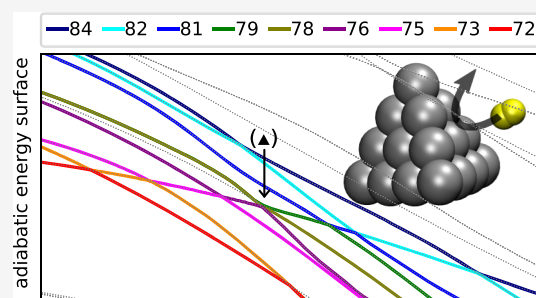


Article Recommendations



Supporting Information

ABSTRACT: We present an efficient set of methods for propagating excited-state dynamics involving a large number of configuration interaction singles (CIS) or Tamm-Dancoff approximation (TDA) single-reference excited states. Specifically, (i) following Head-Gordon et al., we implement an exact evaluation of the overlap of singly-excited CIS/TDA electronic states at different nuclear geometries using a biorthogonal basis and (ii) we employ a unified protocol for choosing the correct phase for each adiabat at each geometry. For many-electron systems, the combination of these techniques significantly reduces the computational cost of integrating the electronic Schrödinger equation and imposes minimal overhead on top of the underlying electronic structure calculation. As a demonstration, we calculate the electronic excited-state dynamics for a hydrogen molecule scattering off a silver metal cluster, focusing on high-lying excited states, where many electrons can be excited collectively and crossings are plentiful. Interestingly, we find that the high-lying, plasmon-like collective excitation spectrum changes with nuclear dynamics, highlighting the need to simulate non-adiabatic nuclear dynamics and plasmonic excitations simultaneously. In the future, the combination of methods presented here should help theorists build a mechanistic understanding of plasmon-assisted charge transfer and excitation energy relaxation processes near a nanoparticle or metal surface.



1. INTRODUCTION

1.1. Molecular Non-Adiabatic Dynamics. Metallic nanoparticles support surface plasmon resonances after illumination, and such collective excitations (involving many high-lying electronic states) can lead to many interesting dynamical phenomena, such as plasmon-mediated reduction and dissociation^{1–3} and plasmon-induced charge transfer.^{4–7} Near a metal surface, the interaction of a molecular system with a continuum of states in a metal can also lead to chemicurrents, unusual vibrational relaxation,^{8,9} and other profoundly non-adiabatic effects. In order to model such essential (but complicated, many-body) phenomena, accurate and efficient tools for simulating coupled electron-nuclei dynamics are sorely needed, especially methods that can accommodate a large number of electronic excited states and many nuclear degrees of freedom. Simulating dozens or hundreds of electronic states with *ab initio* potentials remains a key challenge for physical chemists.^{10–13}

Now, if we seek a molecular description of dynamics near a metal surface, practical considerations dictate that we must employ a semiclassical approach, one whereby we compute the electronic wavefunction using high-level quantum theory but the nuclear wave packet is modeled by an ensemble of classical trajectories. Over the past two decades, beyond Ehrenfest dynamics,^{14,15} a few semiclassical methods have been proposed

to treat dynamics near a metal surface based on Tully's fewest-switches surface hopping (FSSH) algorithm,¹⁶ including independent electron surface hopping (IESH),¹⁷ surface hopping with electronic friction (FSSH-ER),¹⁸ and a broadened classical master equation (BCME).¹⁹ Each of these methods requires propagating trajectories on one surface, with hops between potential energy surfaces to account for electronic relaxation. And in principle, two of these methods (IESH and FSSH-ER) can be combined with *ab initio* electronic structure calculations so as to simulate an arbitrary number of electronic states in the presence of many nuclear degrees of freedom. In practice, however, the computational cost of both IESH and FSSH-ER is very demanding and is determined by how efficiently one can (i) calculate the adiabatic potential energy surfaces and nuclear forces for each time step on the fly (eq 1) and then (ii) propagate an electronic wavefunction spanning

Received: December 27, 2021

Published: May 24, 2022



many, many excited states (eq 3). While the bulk of the time is usually spent on the former (i.e., on the electronic structure calculations), the latter can also add a non-trivial increase to the cost of semiclassical simulations—especially because propagating the latter can dictate the maximum time step allowed in the former.

In this paper, our goal is to present a combination of new tools for efficiently propagating the electronic wavefunction [process (ii) above]. Before we can present the exact protocol, however, we must review the FSSH algorithm for describing coupled electron-nuclei dynamics so that we can highlight the essential problems that must be overcome.

Within FSSH or any FSSH-like algorithm, one always separates the electronic quantum subsystem from the nuclear classical coordinates (\vec{R}, \vec{P}) . The total Hamiltonian for the full system is $\hat{H}(\vec{R}, \vec{P}) = \sum_{\alpha} (P^{\alpha})^2 / 2M^{\alpha} + \hat{H}_{\text{ele}}(\vec{R})$ where $\hat{H}_{\text{ele}}(\vec{R})$ is the electronic Hamiltonian. If we choose a formally diabatic electronic basis, $\{|\Xi_A\rangle, |\Xi_B\rangle, \dots\}$, the matrix elements of the Hamiltonian in such a diabatic basis are defined as $H_{AB}(\vec{R}) = \langle \Xi_A | \hat{H}_{\text{ele}}(\vec{R}) | \Xi_B \rangle$. The electronic Hamiltonian can then be diagonalized to form the adiabatic eigenenergy surfaces $V_j(\vec{R})$ and the corresponding eigenstates $|\Psi^j(\vec{R})\rangle$ satisfying

$$\hat{H}_{\text{ele}}(\vec{R})|\Psi^j(\vec{R})\rangle = V_j(\vec{R})|\Psi^j(\vec{R})\rangle \quad (1)$$

To propagate nuclear dynamics, one assumes that the nuclear coordinates follow Newton's classical equations along a Born–Oppenheimer (BO) surface

$$\frac{\partial R^{\alpha}}{\partial t} = \frac{P^{\alpha}}{M^{\alpha}}; \quad \frac{\partial P^{\alpha}}{\partial t} = -\frac{\partial V_j}{\partial R^{\alpha}} \quad (2)$$

Note that time evolution of the nuclear coordinate $[\vec{R}(t), \vec{P}(t)]$ depicts a classical trajectory moving on the active surface V_j in the nuclear phase space. Along the trajectory, the electronic wavefunction can be expressed as $|\Psi(t)\rangle = \sum_j C_j(t) |\Psi^j(\vec{R}(t))\rangle$ and the quantum amplitude $C_j(t)$ follows the electronic Schrödinger equation

$$i\hbar \frac{\partial C_j}{\partial t} = V_j(\vec{R}(t))C_j - i\hbar \sum_K T_{JK} C_K \quad (3)$$

Here, the time-derivative (**T**) matrix

$$T_{JK} = \left\langle \Psi^J \left| \frac{\partial \Psi^K}{\partial t} \right. \right\rangle \quad (4)$$

characterizes the effect of classical nuclear motion on the quantum electronic subsystem.

1.2. Constructing the Time-derivative **T Matrix.** The necessary ingredients for FSSH are (i) the adiabatic energy surfaces V_j and the nuclear forces $-\partial V_j / \partial R^{\alpha}$ (as calculated at the instantaneous nuclear coordinate $R^{\alpha}(t)$) and (ii) the time-derivative matrix **T** (as constructed from the adiabatic eigenstates of the current and previous time steps). While the on-the-fly calculation of the nuclear forces using electronic structure packages is usually the most computationally intensive step and propagating the electronic wavefunction is relatively fast and cheap, constructing the **T** matrix can also impose expensive overhead on top of the on-the-fly electronic structure calculation, especially for a large number of electronic states. Note that, within any semiclassical scheme, one would like to propagate the classical nuclear coordinates using eq 2 using a larger time step and integrate the electronic Schrödinger equation (eq 3) with a smaller time step. Such a separation of

time steps is essential for large-scale, multidimensional simulations, which makes it essential that the **T** matrix be calculated as accurately as possible (and that one use the **T** matrix as effectively as possible).

Naively speaking, the most straightforward approach to construct the **T** matrix is to compute the derivative coupling between adiabatic states using the usual Hellmann–Feynman expression

$$d_{JK}^{\alpha} = \left\langle \Psi^J \left| \frac{\partial \Psi^K}{\partial R^{\alpha}} \right. \right\rangle = \frac{\left\langle \Psi^J \left| \frac{\partial \hat{H}_{\text{ele}}}{\partial R^{\alpha}} \right| \Psi^K \right\rangle}{V_K - V_J} \quad (5)$$

and then evaluate the **T** matrix element as

$$T_{JK} = \sum_{\alpha} d_{JK}^{\alpha} \frac{P^{\alpha}}{M^{\alpha}} \quad (6)$$

In practice, however, this approach (via the derivative coupling matrix, as given by eq 5) is not efficient. One reason is that the computational cost of evaluating a single derivative coupling d_{JK}^{α} is equivalent to the cost of evaluating a single gradient of the excited state energy surface; thus the cost of constructing the entire derivative coupling matrix between all pairs of states would be exorbitant, equivalent to a quadratic number of expensive gradient calls at each time step. Another reason is that, when the trajectory encounters a so-called trivial crossing^{20,21} (a sharp crossing between two electronic states where the diabatic coupling is effectively zero and a non-adiabatic electronic transition must occur), very small time steps are required to capture the electronic transition.

The first alternative to eq 5 was offered by Hammes-Schiffer and Tully, who suggested an overlap-based propagation scheme that does not rely on the derivative coupling and allows for a larger time step.¹⁷ More recently, Meek and Levine have demonstrated that interpolating the derivative coupling pairwise between adiabatic states (and then averaging the **T** matrix over that time step) provides a better approximation for the case of two electronic states²² and allows for even larger time steps.

$$T_{JK} \left(t + \frac{dt}{2} \right) = \frac{1}{dt} \int_t^{t+dt} d\tau \left\langle \Psi^J(t) \left| U^{\dagger}(\tau) \frac{\partial}{\partial \tau} U(\tau) \right| \Psi^K(t) \right\rangle \quad (7)$$

This approach can be extended to the case of more than two electronic states if we recognized that the **T** matrix can be calculated directly from the logarithm of the overlap matrix²³

$$\mathbf{T} \left(t + \frac{dt}{2} \right) = \frac{1}{dt} \log[\mathbf{U}(dt)] \quad (8)$$

Here

$$U_{JK}(dt) = \langle \Psi^J(t) | \Psi^K(t + dt) \rangle \quad (9)$$

is the overlap matrix of the adiabatic states between two successive time points t and $t + dt$. In practice, the overlap matrix **U** is usually evaluated approximated for a small subspace of electronic states.²⁴

Below, the first focus of the present paper will be the construction of an optimal algorithm for evaluating the **U** matrix of many electronic states with minimal cost. In particular, the first goal of the present paper is to implement an exact method for calculating the overlap matrix of singly-excited states and investigate high-lying excited-state dynamics of a molecule scattering off a metallic nanoparticle. We exploit the

biorthogonal basis technique developed by Sundstrom and Head-Gordon²⁵ and combine it with the protocol for choosing the phase of the adiabatic states. We find that this exact overlap calculation is actually faster by orders of magnitude than the current implementation in most state-of-the-art packages, including Q-Chem and SHARC.²⁶

At this juncture, it is important to emphasize that the sign of a given eigenstate (and the sign of any column in the overlap matrix \mathbf{U}) is undetermined. Moreover, the logarithm of the matrix \mathbf{U} can be very sensitive to these phases of the adiabatic states and changing the signs of a column of the \mathbf{U} matrix can lead to a wildly different \mathbf{T} matrix.^{27,28} To that end, if we wish to run semiclassical non-adiabatic FSSH dynamics, it is crucial to choose the phases of the states in such a way that the \mathbf{T} matrix elements are as smooth as possible, especially when there are many electronic states and many trivial crossings; otherwise, one might need an incredibly small time step to converge. Thus, the second goal of this paper is to implement ref 28 to choose adiabatic eigenstates. As will be reviewed below, ref 28 extends parallel transport to the case of nearly trivial crossings by choosing the optimal phases of the overlap matrix through a simple optimization process.

An outline of this paper is as follows: in Section 2, we show how to group intermediates together so as to construct the overlap \mathbf{U} matrix for CIS or TDA wavefunctions in an efficient way. (Here, we assume we can treat the TDA excitations like real wavefunctions, following ref 29). In Section 3, we implement the optimization process as suggested in ref 28 for dynamically choosing the phases of the overlap matrix. In Section 4, we present results for highly-lying excited-state dynamics of a molecule-nanoparticle system and highlight the performance enhancement of our scheme. We conclude and discuss future applications in Section 5.

Regarding notation, we use \hat{H} to denote a quantum operator and a bold symbol \mathbf{T} to denote a matrix. For classical degrees of freedom, we denote each component of classical vectors with a superscript label as in R^α . We let i, j, k, \dots denote the canonical occupied orbitals, a, b, c, \dots denote the canonical virtual orbitals. Wavefunctions are indexed with capital Roman letters I, J, K, \dots and will usually refer to the CIS/TDA excited states.

2. CONSTRUCTING THE \mathbf{U} MATRIX FOR CIS OR TDA WAVEFUNCTIONS

2.1. CIS (or TDA) Overlap Matrix. To describe electronic excited states, we work in the space of the CIS (or TDA) excitations where one electron in the occupied orbital can be promoted to virtual orbitals. Consider a molecular system with N_o occupied orbitals (ϕ_i) and N_v virtual orbitals (ϕ_a). The Hartree-Fock (HF) ground state is $|\Phi\rangle = |1 \dots N_o\rangle = \det|\phi_1 \dots \phi_{N_o}|$. For a closed-shell system, we assume that the CIS (or TDA) excited states are of the following singlet form

$$|\Psi^J\rangle = \sum_{ia} t_{ia}^J (|\Phi_i^a\rangle + |\Phi_i^{\bar{a}}\rangle) \quad (10)$$

Here, $|\Phi_i^a\rangle$ is a Slater determinant formed by replacing ϕ_i by ϕ_a and t_{ia}^J is the amplitude of the single excitation. In terms of the CIS/TDA excited states, the electronic wavefunction is $|\Psi(t)\rangle = \sum_J C_J(t) |\Psi^J\rangle$. Note that the canonical orbitals (ϕ_i and ϕ_a) and the CIS/TDA amplitudes t_{ia}^J depend on nuclear coordinates \bar{R} .

To construct the overlap matrix $\mathbf{U}(dt)$ at t and $t + dt$, $U_{JK} = \langle \Psi^J | \Psi^K \rangle$, note that the overlap matrix can be expressed as (in the case of a restricted calculation)

$$\langle \Psi^J | \Psi^K \rangle = 2 \sum_{ia} \sum_{j'b'} t_{ia}^J t_{j'b'}^{K'} (\langle \Phi_i^a | \Phi_{j'}^{b'} \rangle + \langle \Phi_i^a | \Phi_{j'}^{\bar{b}'} \rangle) \quad (11)$$

Here, we use an extra prime ($'$) to denote quantities calculated at the second geometry, for example, j', b', K' . Note that $t_{j'b'} = t_{j'\bar{b}'}$ for a restricted calculation (the overbar indicates the opposite spin) and eq 11 requires evaluating the overlap of two singly-excited determinants, $\langle \Phi_i^a | \Phi_{j'}^{b'} \rangle$ and $\langle \Phi_i^a | \Phi_{j'}^{\bar{b}'} \rangle$. As a practical matter, all results below can be easily extended to triplet calculations, unrestricted calculation, or spin-flip calculations. See Supporting Information 4 and 5.

The overlap of two Slater determinants can be evaluated by computing the determinant of the orbital overlap matrix. Let $\{ |p\rangle, p = 1, \dots, N \}$ and $\{ |q'\rangle, q = 1, \dots, N \}$ be two arbitrary sets of orbitals (not necessarily orthonormal). Following refs 30 and 31, the overlap of the two determinants is

$$\langle \dots p \dots | \dots q' \dots \rangle = \det(\mathbf{S}) \quad (12)$$

where the \mathbf{S} matrix is the orbital overlap matrix $S_{pq'} = \langle p | q' \rangle$. Specifically, the HF ground state overlap is

$$\langle \Phi | \Phi' \rangle = \det(\mathbf{S}^o) \quad (13)$$

where $S_{ij}^o = \langle i | j' \rangle$ for $i, j' = 1, \dots, N_o$. The singly-excited determinants can be written as

$$\langle \Phi_i^a | \Phi_{j'}^{b'} \rangle = \det(\mathbf{S}_{ij'}^{ab'}) \quad (14)$$

Here, $\mathbf{S}_{ij'}^{ab'}$ is a square matrix of size N_o , where the i -th orbital is replaced by the virtual orbital a for the geometry at time t and the j' -th orbital is replaced by the virtual orbital b' for the geometry at time $t + dt$.

In most electronic structure calculations, for a given geometry, the canonical orbitals can be chosen to be orthonormal, that is, $\langle i | j \rangle = \delta_{ij}$, $\langle a | b \rangle = \delta_{ab}$, and $\langle i | a \rangle = 0$. However, for different geometries, the canonical orbitals are in general not mutually orthonormal, that is, $\langle i | j' \rangle$ and $\langle a | b' \rangle$ are not diagonal, so that \mathbf{S}_o and $\mathbf{S}_{ij'}^{ab'}$ will be formally dense matrices. As such, when directly constructing the CIS/TDA state overlap matrix, one must evaluate $\det(\mathbf{S}_{ij'}^{ab'})$ (which has computational complexity $O(N_o^3)$) for each element $i, j = 1, \dots, N_o$ and $a, b = 1, \dots, N_v$. In the end, the total computational complexity is $O(N_o^5 N_v^2)$. The key question is how do we most efficiently calculate all of the quantities $\{\det(\mathbf{S}_{ij'}^{ab'})\}$ between two geometries? This item has recently been addressed by refs 32 and 33.

2.2. Method #1: Maximize the Overlap between Orbitals at Two Geometries. Given two different geometries (one "previous" and one "current"), the simplest approach is to rotate the current set of orbitals so that the orbital overlap with the previous geometry is maximized. To do so, we divide the \mathbf{S} matrix into \mathbf{S}^o and \mathbf{S}^v within the occupied and virtual subspaces, respectively, and employ the singular value decomposition (SVD) of the \mathbf{S}^o and \mathbf{S}^v matrices

$$\mathbf{S}^o = \mathbf{U}^o \mathbf{\Lambda}^o \mathbf{V}^{o\dagger} \quad (15)$$

$$\mathbf{S}^v = \mathbf{U}^v \mathbf{\Lambda}^v \mathbf{V}^{v\dagger} \quad (16)$$

Here, the matrix element of the occupied/virtual orbital overlap is given by $S_{ij}^o = \langle i | j' \rangle$ and $S_{ab}^v = \langle a | b' \rangle$, $\Lambda_{ij}^o = \lambda_i^o \delta_{ij}$, and $\Lambda_{ab}^v = \lambda_a^v \delta_{ab}$ are diagonal matrices and \mathbf{U}^o , \mathbf{V}^o , \mathbf{U}^v , and \mathbf{V}^v are unitary matrices (note that \mathbf{U}^o and \mathbf{U}^v are distinct from the overlap matrix \mathbf{U}). At this point, one would like to rotate the orbitals at the second geometry so as to best line up with the orbitals at the

first geometry. As described in Supporting Information 1, this is a well-known problem in applied linear algebra, and the result is (denoting the new orbitals with tildes)

$$|\tilde{j}'\rangle \equiv \sum_{k'l'} |k'\rangle V_{k'l'}^o U_{j'l'}^{o*} \quad (17)$$

$$|\tilde{b}'\rangle \equiv \sum_{c'd'} |c'\rangle V_{c'd'}^v U_{b'd'}^{v*} \quad (18)$$

Here, we emphasize that an overall unitary transformation of the orbitals inside a Slater determinant does not change the state or mix the occupied and virtual subspaces. The CIS/TDA amplitudes can be transformed using the same unitary matrices

$$\tilde{t}_{j'b'}^{K'} = \sum_{k'c'} (\mathbf{U}^v \mathbf{V}^{v\dagger})_{b'c'} t_{k'c'}^{K'} (\mathbf{V}^o \mathbf{U}^{o\dagger})_{j'k'} \quad (19)$$

Therefore, the CIS/TDA state overlap can be written as

$$\langle \Psi^J | \Psi^{K'} \rangle = 2 \sum_{ia} \sum_{j'b'} t_{ia}^J \tilde{t}_{j'b'}^{K'} (\det(\tilde{\mathbf{S}}_{ij}^{ab}) + \det(\tilde{\mathbf{S}}_{ij}^{a\bar{b}})) \quad (20)$$

where we have now defined the overlap matrices in the transformed basis to be $\tilde{\mathbf{S}}$. Note that

$$\tilde{\mathbf{S}}^o = \mathbf{S}^o \mathbf{V}^o \mathbf{U}^{o\dagger} \quad (21)$$

$$\tilde{\mathbf{S}}^v = \mathbf{S}^v \mathbf{V}^v \mathbf{U}^{v\dagger} \quad (22)$$

Furthermore, below, we will at times need the occupied-virtual blocks of the overlap matrix; these blocks are defined to be

$$\tilde{\mathbf{S}}^{ov} = \mathbf{S}^{ov} \mathbf{V}^v \mathbf{U}^{v\dagger} \quad (23)$$

$$\tilde{\mathbf{S}}^{vo} = \mathbf{S}^{vo} \mathbf{V}^o \mathbf{U}^{o\dagger} \quad (24)$$

At this point, we can calculate the determinant of the $\tilde{\mathbf{S}}_{ij}^{ab'}$ matrix. Recall that the $\tilde{\mathbf{S}}_{ij}^{ab'}$ matrix is the occupied block of the transformed matrix ($\tilde{\mathbf{S}}^o$) with the i -th row substituted by $\tilde{S}_{ai} = \langle \tilde{a} | \tilde{l}' \rangle$ ($l' = 1, \dots, N_o$) and the j -th column substituted by $\tilde{S}_{kb} = \langle \tilde{k} | \tilde{b}' \rangle$ ($k = 1, \dots, N_o$). Explicitly, we consider the following two cases

(a) If $i = j$, we can permute the matrix into the following form

$$\tilde{\mathbf{S}}_{ii'}^{ab'} = \begin{pmatrix} \tilde{S}_{ab} & \dots & \tilde{S}_{al|l \neq i} & \dots \\ \vdots & \ddots & & \\ \tilde{S}_{kb|k \neq i} & & \tilde{S}_{kl|k, l \neq i}^o & \\ \vdots & & & \ddots \end{pmatrix} \quad (25)$$

Then, we approximate the determinant by just taking the largest term (i.e., dropping the off-diagonal blocks $\tilde{S}_{al|l \neq i} \approx \tilde{S}_{kb|k \neq i} \approx 0$)

$$\det(\tilde{\mathbf{S}}_{ii'}^{ab'}) \approx \text{Tr} \tilde{\mathbf{S}}^o \frac{\tilde{S}_{ab}}{\tilde{S}_{ii}} \quad (26)$$

(b) If $i \neq j$, we can permute the matrix into the following form

$$\tilde{\mathbf{S}}_{ij'}^{ab'} = \begin{pmatrix} \tilde{S}_{ai} & \tilde{S}_{ab} & \dots & \tilde{S}_{al|l \neq i, j} & \dots \\ \tilde{S}_{ji} & \tilde{S}_{jb} & \dots & \tilde{S}_{jl|l \neq i, j} & \dots \\ \vdots & \vdots & & & \\ \tilde{S}_{ki|k \neq i, j} & \tilde{S}_{kb|k \neq i, j} & & \tilde{S}_{kl|k, l \neq i, j} & \\ \vdots & \vdots & & & \ddots \end{pmatrix} \quad (27)$$

and we approximate the determinant by dropping the off-diagonal blocks

$$\det(\tilde{\mathbf{S}}_{ij'}^{ab'}) \approx \text{Tr} \tilde{\mathbf{S}}^o \frac{\tilde{S}_{ai} \tilde{S}_{jb} - \tilde{S}_{ab} \tilde{S}_{ji}}{\tilde{S}_{ii} \tilde{S}_{jj}} \quad (28)$$

Note that eqs 26 and 28 are very efficient approximations: one throws away many terms in the determinant and instead multiplies together only a few matrix elements. The computational complexity of this step is $O(1)$, which is far cheaper than evaluating the determinant of the dense matrix $\mathbf{S}_{ij}^{ab'}$ of size N_o [which has computational complexity $O(N_o^3)$]. Nevertheless, this approximation rests on the assumption that the relevant set of orbitals does not change much from t to $t + dt$; moreover, one must construct many such orbital overlaps. See Section 2.4 for an analysis of the computational cost of this algorithm.

2.3. Method #2: An Exact Expansion in a Biorthogonal Basis. Rather than rotate one set of orbitals (as in method #1), as shown by Sundstrom and Head-Gordon,²⁵ the better approach is to rotate both sets of orbitals (those at the current and previous geometries) so as to generate a fully biorthogonal basis set. Such an approach has been used previously for several electronic structure calculations^{25,31,34,35} and significantly generalized by Burton.³⁶ Here, we apply this technique to calculate the singly-excited state overlap matrix for use in non-adiabatic dynamics.

Because the required orbital transformation is effectively equivalent to the transformation described in eqs 15 and 16, we will safely use the same notation (superscript tilde) for the new sets of rotated canonical orbitals

$$|\tilde{i}\rangle \equiv \sum_k |k\rangle U_{ki}^o; |\tilde{j}'\rangle \equiv \sum_{l'} |l'\rangle V_{l'j'}^o \quad (29)$$

$$|\tilde{a}\rangle \equiv \sum_c |c\rangle U_{ca}^v; |\tilde{b}'\rangle \equiv \sum_{d'} |d'\rangle V_{d'b'}^v \quad (30)$$

We reiterate that these transformed orbitals are exactly biorthogonal, that is

$$\langle \tilde{i} | \tilde{j}' \rangle = \sum_{kl'} U_{ki}^{o*} \langle kl' | l' \rangle V_{l'j'}^o = \lambda_i^o \delta_{ij'} \quad (31)$$

$$\langle \tilde{a} | \tilde{b}' \rangle = \sum_{cd'} U_{ca}^{v*} \langle cd' | d' \rangle V_{d'b'}^v = \lambda_a^v \delta_{ab'} \quad (32)$$

In other words, within the occupied and virtual subspaces, the transformed orbital overlap matrices \mathbf{S}^o and \mathbf{S}^v are both diagonal. Note that this transformation of the orbitals does not change the HF reference and CIS states (or the DFT Kohn-Sham (KS) reference and TDA states) as one does not mix the occupied and virtual subspaces.

2.3.1. Singly-Excited States Overlap Matrix. With these biorthogonal orbitals in mind, the singly-excited states can be repressed as

$$|\Phi_i^a\rangle = \sum_{kc} U_{ac}^{v*} U_{ik}^o |\Phi_k^c\rangle \quad (33)$$

$$|\Phi_{j'}^{b'}\rangle = \sum_{l'd'} V_{b'd'}^{v*} V_{l'l'}^o |\Phi_{l'}^{d'}\rangle \quad (34)$$

and the overlap matrix is

$$\langle \Phi_i^a | \Phi_{j'}^{b'} \rangle = \sum_{kc} \sum_{l'd'} U_{ik}^{o*} U_{ac}^v \langle \Phi_k^c | \Phi_{l'}^{d'} \rangle V_{b'd'}^{v*} V_{j'l'}^o \quad (35)$$

Next, using eq 12, $\langle \Phi_{\tilde{k}}^{\tilde{c}} | \Phi_{\tilde{l}}^{\tilde{d}'} \rangle$ can be evaluated by calculating the determinant of the biorthogonal orbital overlap matrix

$$\langle \Phi_{\tilde{k}}^{\tilde{c}} | \Phi_{\tilde{l}}^{\tilde{d}'} \rangle = \det(\tilde{\mathbf{S}}_{kl}^{cd'}) \quad (36)$$

Again, the ij -th element of $\tilde{\mathbf{S}}_{kl}^{cd'}$ is equal to the occupied block overlap matrix element $\langle \tilde{i} | \tilde{j}' \rangle$ whenever $i \neq k$ and $j \neq l$; when $i = k$, we must evaluate $\langle \tilde{c} | \tilde{j}' \rangle$ for all j ; when $j = l$, we must evaluate $\langle \tilde{i} | \tilde{d}' \rangle$ for all i . Explicitly, the $\tilde{\mathbf{S}}_{kl}^{cd'}$ matrix can only differ from Λ° (as obtained by the SVD calculation in eq 15) by the k -th row and the l -th column. Note that, in the following equations, k, l and c, d can represent both orbitals and numeric indices. Now, we consider the following two cases:

- (a) If $k = l$, we can permute the orbitals such that the k -th orbital is the first column and row for the orbital overlap matrix, that is

$$\begin{aligned} \tilde{\mathbf{S}}_{kk}^{cd'} &= \langle \dots \tilde{c} \dots | \dots \tilde{d}' \dots \rangle \\ &= \begin{pmatrix} \lambda_c^v \delta_{cd} & \mathbf{Y} |_{k} \\ \mathbf{X} |_{k} & \Lambda^{\circ} |_{k} \end{pmatrix} \end{aligned} \quad (37)$$

Here \mathbf{X} and \mathbf{Y} are the column and row of the occ-vir and vir-occ orbital overlap matrices, respectively

$$X_{md'} \equiv \langle \tilde{m} | \tilde{d}' \rangle \quad (38)$$

$$Y_{cm'} \equiv \langle \tilde{c} | \tilde{m}' \rangle \quad (39)$$

for $m = 1, \dots, N_{\circ}$. The notation $\mathbf{X} |_{k}$ and $\mathbf{Y} |_{k}$ indicate that the k -th element is excluded, that is, $m \neq k$.

To evaluate $\det(\tilde{\mathbf{S}}_{kk}^{cd'})$, we employ the Schur complement of a block matrix (see eq S.7 in Supporting Information 2),

$$\det(\tilde{\mathbf{S}}_{kk}^{cd'}) = \det(\lambda_c^v \delta_{cd} - \mathbf{Y} |_{k} \Lambda^{\circ} |_{k}^{-1} \mathbf{X} |_{k}) \prod_{m \neq k}^{\text{occ}} \lambda_m^{\circ} \quad (40)$$

Explicitly, we have the singly-excited state overlap matrix

$$\begin{aligned} \langle \Phi_{\tilde{k}}^{\tilde{c}} | \Phi_{\tilde{l}}^{\tilde{d}'} \rangle &= \left(\lambda_c^v \delta_{cd} - \langle \tilde{c} | \left(\sum_{m=1}^{\text{occ}} \frac{|\tilde{m}'\rangle \langle \tilde{m}|}{\lambda_m^{\circ}} \right) | \tilde{d}' \rangle + \frac{\langle \tilde{c} | \tilde{k}' \rangle \langle \tilde{k} | \tilde{d}' \rangle}{\lambda_k^{\circ}} \right) \\ &\times \frac{\gamma}{\lambda_k^{\circ}} \end{aligned} \quad (41)$$

where

$$\gamma \equiv \prod_i^{\text{occ}} = \det(\mathbf{S}^{\circ}) \quad (42)$$

- (b) If $k \neq l$, we can build the $\tilde{\mathbf{S}}_{kl}^{cd'}$ matrix from the Λ° matrix by replacing the k -th row by the virtual orbital \tilde{c} and the l -th column by the virtual orbital \tilde{d}' . Again, we can permute the orbitals such that the k and l orbitals are the first two elements for the orbital overlap matrix, that is

$$\begin{aligned} \tilde{\mathbf{S}}_{kl}^{cd'} &= \langle \dots \tilde{c} \dots \tilde{l} \dots | \dots \tilde{k}' \dots \tilde{d}' \dots \rangle \\ &= \begin{pmatrix} \langle \tilde{c} | \tilde{k}' \rangle & \lambda_c^v \delta_{cd} & \mathbf{Y} |_{k,l} \\ 0 & \langle \tilde{l} | \tilde{d}' \rangle & \mathbf{0}^T \\ \mathbf{0} & \mathbf{X} |_{k,l} & \Lambda^{\circ} |_{k,l} \end{pmatrix} \end{aligned} \quad (43)$$

Here $\mathbf{0}$ is a zero column vector of size $N_{\circ} - 2$. Again, we can evaluate $\det(\tilde{\mathbf{S}}_{kl}^{cd'})$ using eq S.7

$$\det(\tilde{\mathbf{S}}_{kl}^{cd'}) = \det \left[\begin{pmatrix} \langle \tilde{c} | \tilde{k}' \rangle & \lambda_c^v \delta_{cd} \\ 0 & \langle \tilde{l} | \tilde{d}' \rangle \end{pmatrix} - \begin{pmatrix} \mathbf{Y} |_{k,l} \\ \mathbf{0}^T \end{pmatrix} \Lambda_{k,l}^{\circ-1} \begin{pmatrix} \mathbf{0} & \mathbf{X} |_{k,l} \end{pmatrix} \right] \prod_{m \neq k,l}^{\text{occ}} \lambda_m^{\circ} \quad (44)$$

Note that the off-diagonal element does not contribute to the determinant. Therefore, for the case where $k \neq l$, we have

$$\langle \Phi_{\tilde{k}}^{\tilde{c}} | \Phi_{\tilde{l}}^{\tilde{d}'} \rangle = \frac{\gamma}{\lambda_k^{\circ} \lambda_l^{\circ}} \langle \tilde{c} | \tilde{k}' \rangle \langle \tilde{l} | \tilde{d}' \rangle \quad (45)$$

Finally, we combine eqs 41 and 45 and write the orbital overlap matrix in the biorthogonal basis as

$$\langle \Phi_{\tilde{k}}^{\tilde{c}} | \Phi_{\tilde{l}}^{\tilde{d}'} \rangle = \gamma \left\langle \tilde{c} \left| \left[\hat{Q} \frac{\delta_{kl}}{\lambda_k^{\circ}} + \frac{|\tilde{k}'\rangle \langle \tilde{l}|}{\lambda_k^{\circ} \lambda_l^{\circ}} \right] \right| \tilde{d}' \right\rangle \quad (46)$$

Here, we define the \hat{Q} operator as

$$\hat{Q} \equiv \hat{I} - \sum_m^{\text{occ}} \frac{|\tilde{m}'\rangle \langle \tilde{m}|}{\lambda_m^{\circ}} \quad (47)$$

Then, we transform the overlap matrix back to the canonical orbital basis by eqs 35 and 30

$$\begin{aligned} \langle \Phi_i^a | \Phi_j^b \rangle &= \gamma \left(\langle a | \hat{Q} | b \rangle \sum_{kl} U_{ik}^{\circ*} \frac{\delta_{kl}}{\lambda_k^{\circ}} V_{jl}^{\circ} \right. \\ &\left. + \sum_{kl} U_{ik}^{\circ*} V_{jl}^{\circ} \frac{\langle a | \tilde{k}' \rangle \langle \tilde{l} | b \rangle}{\lambda_k^{\circ} \lambda_l^{\circ}} \right) \end{aligned} \quad (48)$$

Note that this expression involves the unitary matrix elements ($U^{o/v}$ and $V^{o/v}$) from the SVD.

Next, we introduce auxiliary orbitals (indexed by subscript bars)

$$|\underline{i}'\rangle \equiv \sum_j |j'\rangle \underline{S}_{ij}^{\circ}; \quad |j\rangle \equiv \sum_i |i\rangle \underline{S}_{ij}^{\circ*} \quad (49)$$

where $\underline{S}^{\circ} \equiv ((\mathbf{S}^{\circ})^T)^{-1}$. With the auxiliary orbitals, we can eliminate all dependence on $U^{o/v}$ and $V^{o/v}$, so that we do not have to perform the SVD numerically (see Supporting Information 3). In the end, the singly-excited state overlap matrix can be written as

$$\langle \Phi_i^a | \Phi_j^b \rangle = \gamma (\langle a | \hat{Q} | b \rangle \underline{S}_{ij}^{\circ} + \langle a | \underline{i}' \rangle \langle j | b \rangle) \quad (50)$$

and

$$\langle a | \hat{Q} | b \rangle = \langle a | b \rangle - \sum_k \langle a | \underline{k}' \rangle \langle k | b \rangle \quad (51)$$

For the opposite spin case, notice that $\langle a | \hat{Q} | b \rangle = 0$, so that

$$\langle \Phi_i^a | \Phi_j^{\bar{b}} \rangle = \gamma \langle a | \underline{i}' \rangle \langle \bar{j} | \bar{b} \rangle \quad (52)$$

and in the case of a restricted calculation, the spatial parts of the orbital wavefunctions satisfy $\bar{j} = j, \bar{b} = b$, so that

$$\langle \Phi_i^a | \Phi_j^{\bar{b}} \rangle = \gamma \langle a | \underline{i}' \rangle \langle j | b \rangle \quad (53)$$

Note that, compared to eqs 48, 50–53 depend on only the bare \mathbf{S} matrix, rather than relying on \mathbf{U}^o , \mathbf{V}^o , and λ_k^o from the SVD calculation (eq 15). Therefore, we need only the bare \mathbf{S} matrix in order to construct the exact singly-excited state overlap matrix.

2.3.2. CIS/TDA Overlap Matrix. To calculate the CIS/TDA overlap matrix element, we insert eqs 50 and 53 into eq 11

$$\langle \Psi^J | \Psi^{K'} \rangle = 2\gamma \left(\sum_{ab} \langle a | \hat{Q} | b' \rangle \sum_{ij} t_{ia}^J t_{j'b'}^{K'} S_{ij}^o + 2 \sum_{ia} t_{ia}^J \langle a | \underline{i}' \rangle \sum_{jb} t_{j'b'}^{K'} \langle j | b' \rangle \right) \quad (54)$$

For simplicity, we write the virtual orbitals in terms of the auxiliary orbitals as

$$W_{ai} \equiv \langle a | \underline{i}' \rangle = \sum_j \langle a | j' \rangle (S^o)_{ji}^{-1} \quad (55)$$

$$Z_{jb} \equiv \langle j | b' \rangle = \sum_i (S^o)_{ji}^{-1} \langle i | b' \rangle \quad (56)$$

$$Q_{ab} \equiv \langle a | \hat{Q} | b' \rangle = \langle a | b' \rangle - \sum_k W_{ak} \langle k | b' \rangle \quad (57)$$

Then, we define the following quantities that depend on the CIS/TDA coefficients

$$A^{JK} \equiv \sum_{ia} \sum_{jb} t_{ia}^J t_{j'b'}^{K'} Q_{ab} (S^o)_{ji}^{-1} \quad (58)$$

$$B^J \equiv \sum_{ia} t_{ia}^J W_{ai} \quad (59)$$

$$C^K \equiv \sum_{jb} t_{j'b'}^{K'} Z_{jb} \quad (60)$$

In the end, the final expression for the CIS/TDA overlap matrix element is

$$\langle \Psi^J | \Psi^{K'} \rangle = 2\gamma [A^{JK} + 2B^J C^K] \quad (61)$$

As a final note, we emphasize that method #2 is not limited to restricted closed-shell wavefunction calculations: for the unrestricted Hartree-Fock cases, see Supporting Information 4; for the spin-flip variants of CIS and TD-DFT,^{37,38} see Supporting Information 5.

2.3.3. Algorithmic Summary. In this section, we summarize the algorithm to construct the CIS/TDA state overlap between two different geometries $\langle \Phi | \Phi^{K'} \rangle$

1. Build the canonical orbital overlap matrix between two different geometries: $S_{ij} = \langle i | j' \rangle$, $S_{ab} = \langle a | b' \rangle$, and the occ-
vir overlap $S_{ia} = \langle i | a' \rangle$.
2. Consider the occupied subspace and calculate $\gamma = \det(\mathbf{S}^o)$.
3. Project the virtual orbitals into the basis of auxiliary orbitals by solving the linear equations in eqs 55 and 56; evaluate Q_{ab} using eq 51. Note that, since W_{ai} , Z_{jb} , Q_{ab} do not depend on the CIS/TDA states, one needs to calculate these quantities just once for each time step.
4. For each pair of CIS/TDA states J, K , evaluate A^{JK} , B^J , and C^K using eqs 58–60. Then, put them all together according to eq 61.

2.4. Computational Complexity. At this point, let us turn our attention to the computational complexity of evaluating the CIS/TDA overlap matrix $\langle \Psi^J | \Psi^{K'} \rangle$ using the above methods. To compare the computational complexity, we assume the \mathbf{S}^o and \mathbf{S}^v matrices are known and $O(N_o) \approx O(N_v) \approx O(N_s)$ are of the same order of magnitude $\approx O(N)$. As a reference, a straightforward approach requires two steps: (I) evaluating the determinant of the canonical orbital overlap matrix for every $\mathbf{S}_{ij}^{ab'}$ matrix (eq 14), which takes $O(N_o^5 N_v^2)$; (II) computing the summation in eq 11 for every element $\langle \Psi^J | \Psi^{K'} \rangle$, which takes $O(N_s N_o^2 N_v^2 + N_s^2 N_o N_v)$. Therefore, if we compute the CIS/TDA overlap matrix naively, the total computational complexity is dominated by the leading order $O(N_o^5 N_v^2) \approx O(N^7)$ in step (I).

2.4.1. Method #1. Method #1 takes the following steps:

- (i) Two SVD calculations (eqs 15 and 16), which requires $O(N_o^3 + N_v^3)$;
- (ii) Matrix multiplication for generating the $\tilde{\mathbf{S}}$ matrix (eqs 21–24), which requires $O(N_o^3 + N_v^3 + N_o^2 N_v + N_v^2 N_o)$. Note that, once $\tilde{\mathbf{S}}$ is constructed, evaluating the approximate determinant using eqs 26 and 28 is $O(1)$;
- (iii) Transformation of the amplitude $t_{j'b'}^{K'}$ for every CIS/TDA state using eq 19, which takes $O(N_s N_o N_v^2 + N_s N_s^2 N_v)$;
- (iv) Evaluation of the summation in eq 20 for every J and K , which takes $O(N_s N_o^2 N_v^2 + N_s^2 N_o N_v)$.

Note that, because we approximately evaluate the determinant of the orbital overlap matrix in step (ii), the most expensive step is now the summation in step (iv). Therefore, the leading order of computational complexity for Method #1 is $O(N_s N_o^2 N_v^2) \approx O(N^5)$; in other words, method #1 reduces the cost of the algorithm by 2 orders of magnitude relative to a naive, straightforward approach.

2.4.2. Method #2. Method #2 takes the following steps:

- (i') Evaluation of the determinant of \mathbf{S}^o to compute the coefficient γ using eq 42, which takes $O(N_o^3)$;
- (ii') Solving linear equations for W_{ai} and Z_{jb} in eqs 55 and 56; both steps require $O(N_o^2 N_v)$ work;
- (iii') Matrix multiplication for constructing the \mathbf{Q} matrix using eq 57, which requires $O(N_v^2 N_o)$ cost;
- (iv') Constructing the A^{JK} matrix using eq 58. Here, the summation $\sum_{ia,jb}$ can be decomposed into $\sum_i t_{ia}^J (S^o)_{ji}^{-1}$ (of order $O(N_s N_v N_o^2)$) and $\sum_b t_{j'b'}^{K'} Q_{ab}$ (of order $O(N_s N_o N_v^2)$). Thus, constructing the A^{JK} matrix requires $O(N_s N_o^2 N_v + N_s N_o N_v^2 + N_s^2 N_o N_v)$;
- (v') Computing the B^J and C^K using eqs 59 and 60, both of which have cost $O(N_s N_o N_v)$.

We emphasize that method #2 can evaluate the exact determinant of the orbital overlap matrix [steps (i')–(iii')] at the same order of computational cost as in method #1, but does not rely on approximating the orbital determinants. More importantly, by design, the key advantage of method #2 is the decomposition of the summation in eq 11 into two cheaper factorized summations (A^{JK} and $B^J C^K$) as in Steps (iv') and (v'). Therefore, the computational complexity of method #2 is $O(N_s N_o^2 N_v + N_s N_o N_v^2 + N_s^2 N_o N_v) \approx O(N^4)$; by contrast, recall that method #1 has a computational cost of $O(N^5)$.

3. CHOOSING THE PHASES OF ADIABATIC STATES

The second goal of this paper is to implement the optimization approach described in ref 28 for choosing the phases of the adiabatic states. For a real-valued electronic Hamiltonian, to

smoothly propagate the electronic wavefunction using the overlap-based scheme, the overlap matrix at each time step must be a proper rotation matrix with a real matrix logarithm. Mathematically, a necessary condition for any matrix to be a proper rotation matrix is $\det(\mathbf{U}) = 1$. Now, if we ever find that, in practice, $\det(\mathbf{U}) \neq 1$, we may conclude that there must be one (or an odd number of) negative eigenvalue(s) corresponding to an eigenstate that flips its sign from the previous geometry, meaning that the phase of the adiabatic state is not continuous.

With this necessary condition in mind, the optimal phase of the overlap matrix should be chosen dynamically at each time step so as to minimize the norm of the \mathbf{T} matrix ($\sum_{JK} |T_{JK}|^2$ or equivalently $\text{Tr} \log \mathbf{U}^2$). In principle, we can change the signs of the columns of the \mathbf{U} matrix to find the optimal matrix with the minimal norm. However, such a direct brute-force search would require 2^{N_s} matrix logarithm evaluations, which is very expensive for many electronic states. Therefore, instead of the direct minimization, there are several protocols for choosing the phases.

3.1. Maximally Positive (MP) Approach. The maximally positive approach is a straightforward extension of parallel transport where one chooses the phase of adiabatic states to make all diagonal matrix elements of the overlap matrix (U_{JJ}) real and maximally positive. Explicitly, the MP protocol can be implemented at each time step as follows

1. For each column J , if $U_{JJ} < 0$, we flip the sign of the J -th column.
2. In the end, if $\det(\mathbf{U}) < 0$, we find the column with the smallest diagonal element (i.e., $|U_{J_0 J_0}| \leq |U_{JJ}|$ for all J) and flip the sign of the J_0 -th column.

Note that making all diagonal elements positive may correspond to $\det(\mathbf{U}) = -1$, which is incompatible with a pure rotation of adiabatic states.²⁸ In particular, in the extreme non-adiabatic limit of curve crossings (such as a trivial crossing) or in the case where more than two states cross at the same time, one may find the diagonal element of the overlap matrix can be zero (especially when the classical time step is large), which makes parallel transport unstable and ambiguous; in such a case, there is no reason at all to presume that $\det(\mathbf{U}) = 1$. Therefore, changing the sign of the column with the smallest diagonal element (i.e., maximally positive) is a straightforward fix to ensure $\det(\mathbf{U}) = 1$. This being said, we emphasize that such a change does not minimize the norm $\text{Tr} \log \mathbf{U}^2$, and the time derivative \mathbf{T} matrix may not always be optimally smooth for a large time step. In principle, if one uses a very small time step and many grid points, the MP protocol can recover smooth wavefunction propagation and capture the correct electronic transition, but we expect that the need for such small time steps will make calculations more expensive than our optimized approach.

3.2. Optimization (OP) Approach. Recently, our group has developed an alternative optimization protocol for choosing the optimal phase of the adiabatic states. Basically, instead of evaluating the matrix logarithm $\text{Tr} \log \mathbf{U}^2$ 2^{N_s} times, we minimize a polynomial function of \mathbf{U} ($\text{Tr}(3\mathbf{U}^2 - 16\mathbf{U})$ for a real overlap matrix \mathbf{U}) using Jacobi sweeps. Note that the target function, $\text{Tr}(3\mathbf{U}^2 - 16\mathbf{U})$, is a second order approximation of $\text{Tr} \log \mathbf{U}^2$ around $\mathbf{U} = \mathbf{I}$. Explicitly, the OP protocol can be implemented at each time step as follows:

1. If $\det(\mathbf{U}) < 0$, we change the sign of the first eigenvector.
2. For each pair J, K , we minimize

$$\text{Re}(\text{Tr}(3\mathbf{U}^2 - 16\mathbf{U})) \quad (62)$$

by calculating the difference Δ_{JK} defined as

$$\begin{aligned} \Delta_{JK} = & 3(U_{JJ}^2 + U_{KK}^2) + 6U_{JK}U_{KJ} + 8(U_{JJ} + U_{KK}) \\ & - 3 \sum_L (U_{JL}U_{LJ} + U_{KL}U_{LK}) \end{aligned} \quad (63)$$

If $\Delta_{JK} < 0$, we flip the signs of the J -th and K -th columns simultaneously.

3. Return to step 2 until all $\Delta_{JK} > 0$.

Note that, if we start with a \mathbf{U} with $\det(\mathbf{U}) = 1$, then at every iteration, we flip the signs of a pair of columns in the \mathbf{U} matrix in order to preserve the condition $\det(\mathbf{U}) = 1$. In ref 28, we demonstrated that this optimization approach yields the time-derivative coupling matrix elements that are as smooth as possible. Note that the optimization approach has the computational complexity $O(N_s^2)$, which is almost instantaneous in comparison to constructing the CIS/TDA state overlap matrix. By design, our hope has been that the OP protocol should allow for a larger time step dt_c .

4. RESULTS AND DISCUSSION

With these computational tools, we will analyze a test case of excited state electronic dynamics for a system involving many electronic states. Consider a molecule-nanoparticle system with a H_2 molecule scattering off a tetrahedral silver metal nanoparticle Ag_{20} . The initial position of the H_2 molecule is 7.3 Å away from the center of the metal cluster. The Ag_{20} cluster is set to be static initially, and the initial kinetic energy of the H_2 molecule is $E_{K_0} = m_p |v_0|^2 = 0.15$ eV, where $m_p \approx 1836m_e$ is the proton mass and the initial velocity ($v_0 = 0.001$ a.u.) is moving toward the origin.

As reported in past work,³⁹ such a silver metal cluster supports surface plasmon resonance at the excitation energy ~ 3.59 eV, which involves collective electronic transitions and shows a large oscillation strength in the absorption spectrum. This plasmonic excitation is much higher than the HOMO–LUMO gap (~ 1.68 eV) of the metal cluster. Therefore, we expect that excited state dynamics may well populate many high-lying electronic states.

4.1. Simulation Details. The optimized geometry of the tetrahedral Ag_{20} cluster is centered at the origin and adopted from ref 39. We employ time-dependent density functional theory (TDDFT) to calculate excited states using the PBE exchange functional and Tamm-Dancoff approximation (TDA). We use the 6-31G basis for the hydrogen molecule and employ the Couty-Hall modified LANL2DZ basis sets (modified-LANL2DZ) with an effective core potential for the silver cluster.⁴⁰ The first $N_s = 128$ singlet excitations are computed, and the numbers of the occupied/virtual orbitals are $N_o = 191$ and $N_v = 253$. We use the Q-Chem package for the electronic structure and dynamics calculations.¹² Note that we consider only singlet states as generated from a restricted DFT KS ground state. The overlaps between the TDA excited states are calculated just as they would be for the CIS states following ref 29. Due to the spatial symmetry of the tetrahedral geometry of the metal nanoparticle, there are many degenerate states and we can easily find trivial crossings with more than two states.

Because our focus here is on the evolution of the electronic wavefunction, we will make the strong assumption that all nuclear coordinates are propagated on the ground state using the velocity Verlet method. We also neglect any non-adiabatic

effects on the nuclear motion. The propagation of the electronic nuclei dynamics is implemented using two different time steps. For the nuclear degrees of freedom, the ground state nuclear dynamics is evolved using the classical time step dt_c ; the overlap \mathbf{U} matrix and the time-derivative \mathbf{T} matrix are evaluated by comparing the two geometries before and after the classical time step. For the electronic dynamics, the electronic Schrödinger equation (eq 3) is integrated using the fourth-order Runge–Kutta method with a substantially smaller quantum time step (here, we choose $dt_q = dt_c/50$) and using the \mathbf{T} matrix above. Note that, once we have the \mathbf{T} matrix, propagating the electronic amplitudes is usually very cheap (in comparison to calculating the overlap matrix).

4.2. Method #2 Outperforms Method #1 by Orders of Magnitude. In Figure 1, we compare the computational

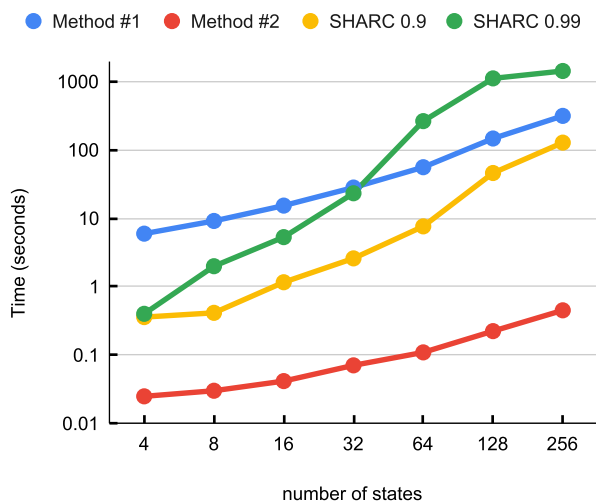


Figure 1. Walltime on 32 cores for constructing the TDA state overlap matrix $\langle \Phi^j | \Phi^{k'} \rangle$ using method #1 and #2 and SHARC^{26,32} is plotted in a logarithmic scale as a function of the number of electronic states. In general, we find that method #2 (red) is at least 2 orders of magnitude faster than method #1 (blue). For the SHARC routine, the overlap matrix is constructed by predetermining a certain percentage of the determinants to be evaluated with eq 11. Here, we denote SHARC 0.9 (0.99) for the results where 90% (99%) of the determinants are evaluated. For $N = 256$ states, method #2 can be more than 3 orders of magnitude faster than SHARC 0.99. Recall that method #2 is exact.

expenses of constructing the overlap matrix by method #1 versus method #2. In particular, we compare the walltime for calculating the TDA state overlap at different times by eq 11 using 32 CPU cores. We find that the performance of method #2 is faster than method #1 by orders of magnitude, especially for a large number of electronic states. In fact, as shown in Figure 1, method #2 (red) can be ≈ 700 times faster than method #1 (blue) when we construct the overlap matrix for $N_s = 256$ TDA states. As a point of comparison, the current algorithm is also faster than the corresponding overlap in SHARC.^{26,32}

4.3. Choosing the Proper Phase of the Overlap Matrix Accelerates the Convergence with Respect to dt_c . With the overlap matrix as constructed using method #2, we now turn our attention to choosing the phase of the overlap matrix. Here, we compare the electronic state population dynamics as obtained by integrating the electronic Schrödinger equation (eq 3) using different phase protocols. At each time step, the phase of the overlap matrix $\mathbf{U}(dt_c)$ is determined following either the OP protocol or the MP protocol. Note that, when

decreasing the classical time step dt_c , one expects that both protocols should converge and agree with each other in the extremely small dt_c limit.

To compare between the OP and MP protocols, we initialized the electronic wavefunction to be on state $J = 72$ (i.e., $P_{72} = 1$ at $t = 0$). This representative trajectory will encounter several interesting scenarios.

4.3.1. Trivial Crossing with a Pure State Wavefunction. In Figure 2, we plot the relative adiabatic states and the electronic

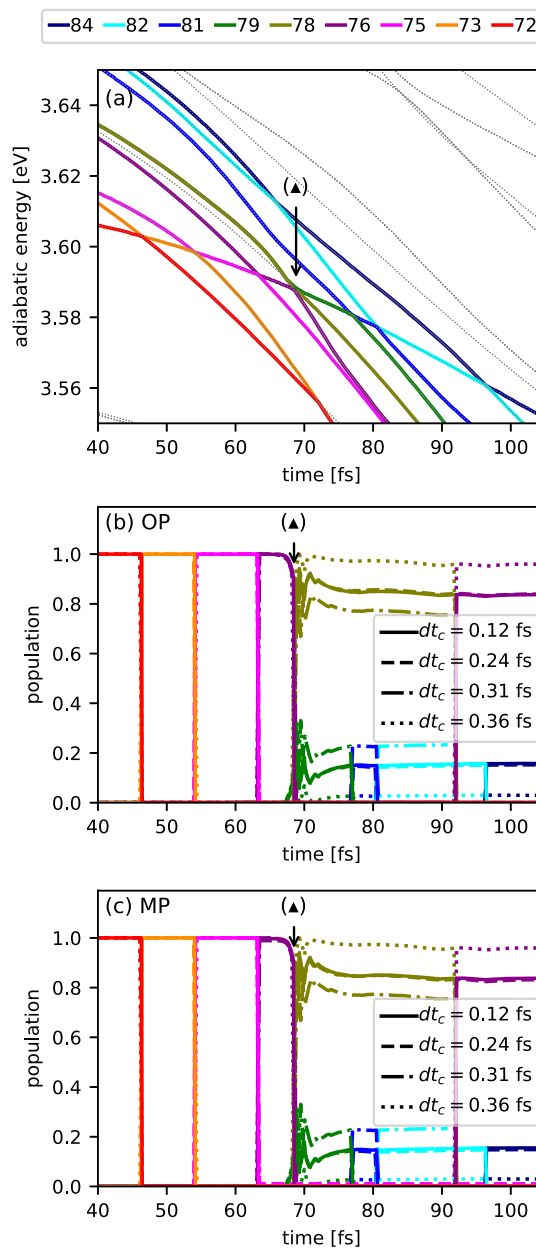


Figure 2. (a) Adiabatic potential energy surfaces and the electronic population dynamics following the (b) OP protocol and (c) MP protocol are plotted as a function of time for different classical time steps dt_c . The initial electronic wavefunction is an adiabatic state $J = 72$ (red lines). The relevant surfaces (where the corresponding populations are non-zero) are colored. (\blacktriangle) indicates a three state crossing ($76 \rightarrow 78, 79$) at $t = 68.8$ fs. After the three state crossing, the wavefunction becomes a superposition state with $P_{78} \approx 0.85$ and $P_{79} \approx 0.15$. Note that, up to $t = 105$ fs, the results of the OP and MP protocols agree with each other and both are converged for $dt_c = 0.24$ fs.

populations according to the OP and MP protocols for the first 105 fs of the trajectory. First, in subplot (a), notice that the energy surface for the $J = 72$ state (red line) has a trivial crossing with the $J = 73$ state around 46.5 fs; the electronic population makes a complete transition ($72 \rightarrow 73$). In fact, there are three trivial crossings occurring before $t = 65$ fs. Importantly, for all of these trivial crossings, the initial electronic wavefunction begins and ends on one adiabatic state. For this reason, we find that both the MP and OP protocols can capture the correct transition even with a large classical time step (such as $dt_c = 0.36$ fs). Intuitively, this result is not surprising: the phase of the overlap matrix does not affect the electronic wavefunction propagation when the propagation involves just two states.

This being said, when there is a three state crossing [e.g., $76 \rightarrow 78, 79$ at $t = 68.8$ fs as labeled by the black triangle (\blacktriangle) in Figure 2], the electronic transition becomes more complicated. Here, after the crossing at (\blacktriangle), the electronic population becomes $P_{78} \approx 0.85$ and $P_{79} \approx 0.15$ (i.e., the wavefunction is a superposition of the TDA states of $J = 78, 79$). This crossing is non-trivial, and a small time step is required to capture the correct electronic transition probability (here, $dt_c = 0.24$ fs is sufficient). For this three state crossing, we find that the propagation following the OP and MP protocols are almost the same and both algorithms converge to the correct results for $dt_c = 0.24$ fs.

4.3.2. Trivial Crossing with a Superposition Wavefunction.

In Figure 3, we continue the propagation in Figure 2, now plotting populations from 105 fs through 145 fs. We emphasize however, that, after 69 fs, the electronic wavefunction is a superposition of adiabatic TDA states. In general, the more states that are populated and the more relative phases there are to keep track of, the more we expect the OP and MP protocols may differ. Indeed, Figure 3 shows that the OP and MP protocols differ for $dt_c = 0.24$ fs. This being said, as dt_c decreases, the population dynamics following the OP protocol converges for $dt_c = 0.17$ fs (see Figure 3b); however, the MP protocol does not converge even for $dt_c = 0.12$ fs (see Figure 3c). We must now explain this difference in convergence.

To understand the underlying differences between the OP and MP protocols, let us focus on the trivial crossing at $t = 110.5$ fs as labeled by the black square (\blacksquare) in Figure 3. We observe that, for an incoming superposition state wavefunction, the electronic transition between states 74 (orange line) and 75 (magenta line) affects the relative phases of the other states (here 84 blue line). For $dt_c = 0.24$ fs at (\blacksquare), the overlap matrix following the OP protocol is (for states 74, 75, and 84)

$$\mathbf{U}_{\text{OP}} = \begin{pmatrix} 0.0 & -0.99987 & \cdots & 0.0 \\ 0.99999 & 0.0 & \cdots & -0.00011 \\ \vdots & & & \\ 0.00011 & & & \end{pmatrix}$$

and the overlap matrix following the MP protocol is (for states 74, 75, and 84)

$$\mathbf{U}_{\text{MP}} = \begin{pmatrix} -0.0 & -0.99987 & \cdots & 0.0 \\ -0.99999 & 0.0 & \cdots & -0.00011 \\ \vdots & & & \\ -0.00011 & & & \end{pmatrix}$$

Here, we notice that the MP protocol flips the sign of column 74 of the overlap matrix to ensure $\det(\mathbf{U}_{\text{MP}}) = 1$, leading to

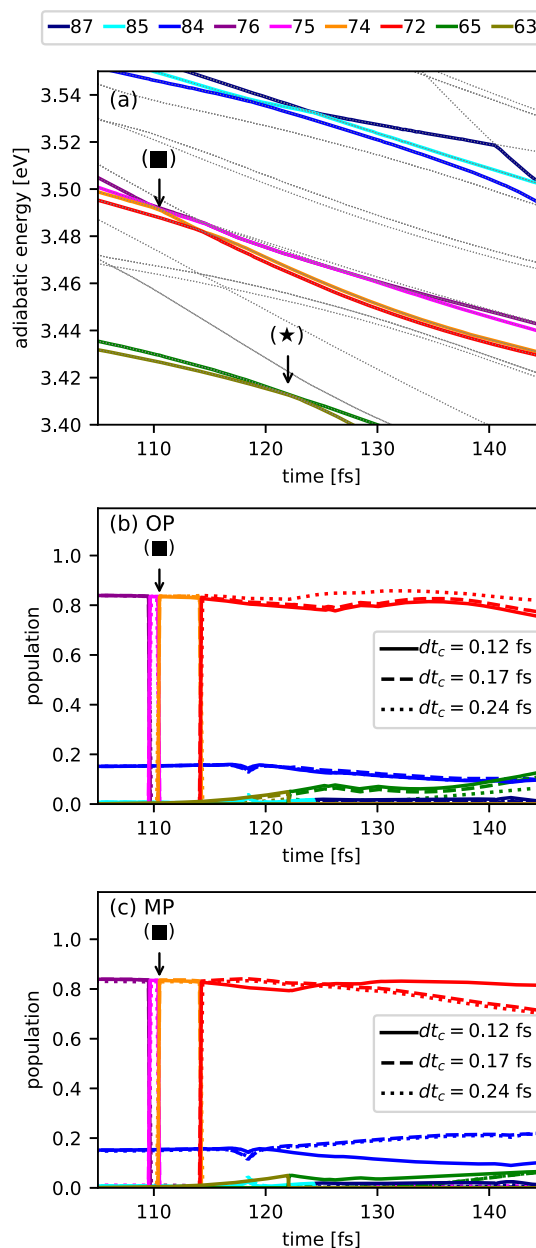


Figure 3. Continuation of Figure 2 for longer times. (a) Adiabatic potential energy surfaces and the electronic population dynamics following the (b) OP protocol and (c) MP protocol are plotted as function of time for different classical time steps dt_c . (\blacksquare) and (\star) indicate trivial crossings of two states where the electronic wavefunction is a superposition state and has non-zero coefficients for other TDA states. At (\blacksquare), there is a complete electronic transition from state 75 (magenta) to state 74 (orange), while the coefficient of state 84 (blue) is nonzero with a relative phase of importance. The OP protocol preserves this relative phase and converges to the correct dynamics when $dt_c = 0.17$ fs. However, the MP protocol disturbs this relative phase leading to incorrect long time dynamics and cannot converge even for $dt_c = 0.12$ fs. In the end, using the OP protocol allows for using at least 40% larger classical time step than the MP protocol.

changing the sign relative to states 84. (The two protocols also differ by a sign in column 122 at this point in time, but this adiabat is not populated and so is of no consequence.) While this relative sign discrepancy does not lead to a difference in populations for 10 fs (i.e., until $t = 120$ fs), this difference will

eventually lead to dramatic differences when yet another crossing is encountered.

In Figure 4, we compare results for the OP and MP protocols for the smallest time step we treated, $dt_c = 0.12$ fs. We find that,

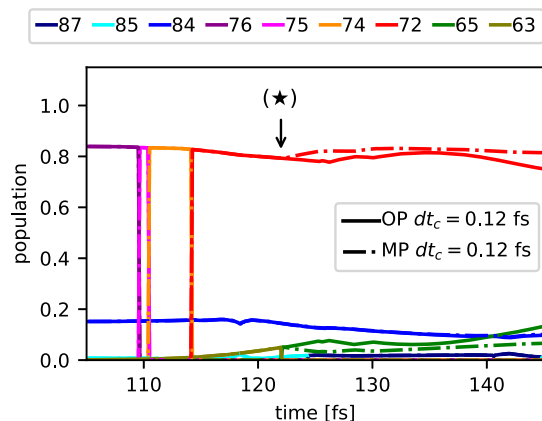


Figure 4. Population dynamics for the OP protocol (solid lines) versus the MP protocol (dash-dot lines) using the smallest time step size tested ($dt_c = 0.12$ fs in Figure 3). The OP and MP protocol agree with each other before $t = 122$ fs as labeled by (★). Note that the MP protocol does not yield the correct phase for the overlap matrix at (★), which leads to incorrect dynamics, suggesting that one would need an even smaller time step for the MP protocol to converge.

through $t = 120$ fs or so, we find that the population dynamics of state 84 are the same for both protocols, from which one must conclude that $dt_c = 0.12$ fs is sufficiently small for the MP protocol to recover the correct overlap matrix at (■). However, at $t = 122$ fs (★), the population dynamics following the OP and MP protocol differ for states 65 and 72, even for with a very small time step. This discrepancy arises because another crossing is encountered, whereby the interaction of states 63 and 65 disturbs the relative phase of state 72. This disturbance eventually leads to a big difference in population for long times ($P_{84} = 0.08$ for the OP protocol versus $P_{84} = 0.21$ for the MP protocol at $t = 145$ fs).

Lastly, to confirm that the converged OP protocol is indeed more physical than the MP protocol, we can check the norm of the T matrix at the $t = 122$ fs crossing as labeled by the black star (★) and evaluate $\text{Tr}\{|\log \mathbf{U}|^2\}$ for each method, respectively. We find

$$\text{Tr}\{|\log \mathbf{U}_{\text{OP}}(t = 122, dt_c = 0.12)|^2\} = 14.01,$$

$$\text{Tr}\{|\log \mathbf{U}_{\text{MP}}(t = 122, dt_c = 0.12)|^2\} = 22.23$$

Note that the OP protocol indeed has smaller $\text{Tr}\{|\log \mathbf{U}|^2\}$, meaning that the T matrix as chosen by the OP protocol is smoother and closer to “parallel transport” than is the MP protocol.

In the end, for this very simple problem, our results show that the OP approach can use a 40% larger classical time step (which should lead to at least 40% speedup). These results emphasize that choosing the optimal phase is important, especially for systems with many electronic states.

4.4. High-Lying Excitation Spectrum Becomes Dynamic after the Collision. With the efficient integration scheme for the electronic Schrodinger equation in place, we are now ready to analyze the high-lying excited state dynamics of the H_2 - Ag_{20} scattering problem. First, we focus on the TDA

excitation spectrum. At this level of theory, the spectrum of a tetrahedral Ag_{20} nanoparticle has a strong peak around ≈ 3.56 eV, which originates from a collective electronic excitation in analogy to a localized surface plasmonic resonance. Since our initial geometry positions the H_2 molecule far away from Ag_{20} , the initial spectrum (Figure 5a) almost replicates the spectrum of an isolated Ag_{20} cluster.

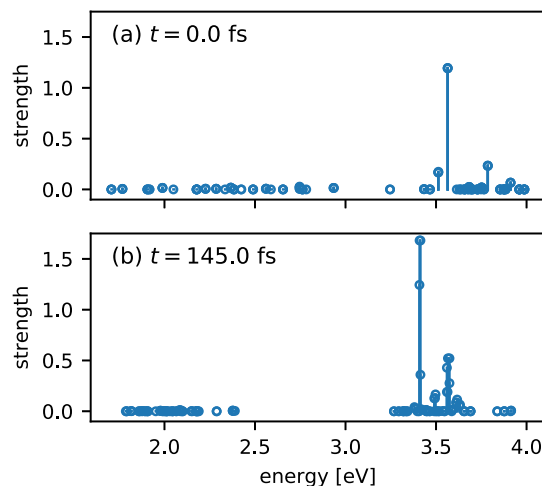


Figure 5. (a) Initial spectrum of the H_2 - Ag_{20} system where the strongest oscillator strength peak (≈ 3.56 eV) corresponds to a plasmonic excitation of the Ag_{20} cluster, involving multiple single electron excitations; in other words, the TDA state is a linear combination of many $|\Phi_i^e\rangle$. (b) Final spectrum at time $t = 145$ fs, significantly after the scattering event. Note that the strongest peak (≈ 3.41 eV) is no longer a collective excitation; the plasmon has moved to 3.57 eV.

Second, after the H_2 collision (occurring at $t \approx 70$ fs), we continue to propagate the classical nuclear dynamics so that the H_2 molecule eventually moves far away from Ag_{20} again. However, the silver cluster is now excited and vibrating; the excitation spectrum is now changing in time. In (Figure 5b), we plot the spectrum at time $t = 145$ fs. Notice that the strongest peak has shifted to 3.41 eV and an additional second (strong) peak has emerged around 3.61 eV. Interestingly, by comparison with the spectrum before collision, the strongest peak now involves only single electron excitation, rather a collective excitation, whereas the second strongest peak now is a plasmon-like collective excitation (rather than a single electron excitation). These conclusions highlight the need to model both nuclear dynamics and plasmonic excitations at the same time.

5. CONCLUSIONS

We have formulated an efficient algorithm for propagating excited-state wavefunctions involving many electronic states using well-established overlap-based methods²³ and phase conventions.²⁸ In particular, we have combined an exact method for constructing the overlap matrix for CIS/TDA wavefunctions using a bi-orthogonal basis with an optimization protocol for choosing the proper phase of adiabatic states. We applied the resulting algorithm to investigate the high-lying excited-state dynamics of a large electronic system with many trivial crossings and degenerate states. Our results show that use of the bi-orthogonal basis can accelerate the construction of the overlap matrix by orders of magnitude at each time step, and that

choosing the optimal phase of the overlap matrix allows for a larger classical time step for the propagation. Altogether, large savings can be accrued.

Looking forward, the present algorithm has been applied to a scattering process of a hydrogen molecule from a metal nanocluster. Altogether, the calculations presented here requires on the order of three days of computational time on one node with 32 CPU cores. In the future, our goal will be to apply the present method to begin assessing non-adiabatic dynamics near plasmonic surfaces, which is nowadays a rather “hot” topic in physical chemistry.¹³

■ ASSOCIATED CONTENT

SI Supporting Information

The Supporting Information is available free of charge at <https://pubs.acs.org/doi/10.1021/acs.jctc.1c01304>.

The Supporting Information includes: Overlap maximization scheme, useful identity for computing determinants using the Schur complement, auxiliary overlap and orbitals, overlaps for unrestricted CIS or TDDFT/TDA states, and overlaps for spin-flip CIS or TDDFT/TDA states (PDF)

■ AUTHOR INFORMATION

Corresponding Author

Hsing-Ta Chen – Department of Chemistry, University of Pennsylvania, Philadelphia, Pennsylvania 19104, United States; orcid.org/0000-0002-6619-1861; Email: hchen@sas.upenn.edu

Authors

Junhan Chen – Department of Chemistry, University of Pennsylvania, Philadelphia, Pennsylvania 19104, United States; orcid.org/0000-0003-4843-6324

D. Vale Cofer-Shabica – Department of Chemistry, University of Pennsylvania, Philadelphia, Pennsylvania 19104, United States

Zeyu Zhou – Department of Chemistry, University of Pennsylvania, Philadelphia, Pennsylvania 19104, United States

Vishikh Athavale – Department of Chemistry, University of Pennsylvania, Philadelphia, Pennsylvania 19104, United States; orcid.org/0000-0002-0571-2336

Gregory Medders – Department of Chemistry, University of Pennsylvania, Philadelphia, Pennsylvania 19104, United States; orcid.org/0000-0001-8988-4401

Maximilian F. S. J. Menger – Zernike Institute for Advanced Materials, Faculty of Science and Engineering, University of Groningen, Groningen 9747AG, The Netherlands; orcid.org/0000-0003-1442-9601

Joseph E. Subotnik – Department of Chemistry, University of Pennsylvania, Philadelphia, Pennsylvania 19104, United States

Zuxin Jin – Division of Chemistry and Chemical Engineering, California Institute of Technology, Pasadena, California 91125, United States; orcid.org/0000-0002-1533-3348

Complete contact information is available at <https://pubs.acs.org/doi/10.1021/acs.jctc.1c01304>

Notes

The authors declare no competing financial interest.

■ ACKNOWLEDGMENTS

We thank Christine Aikens for providing the tetrahedral geometries of the silver cluster. This work has been supported by the U.S. Department of Energy, Office of Science, Office of Basic Energy Sciences, under Award no. DE-SC0019397 (JES). It also used resources of the National Energy Research Scientific Computing Center (NERSC), a U.S. Department of Energy Office of Science User Facility operated under Contract no. DE-AC02-05CH11231.

■ REFERENCES

- (1) Lee, S. J.; Piorek, B. D.; Meinhart, C. D.; Moskovits, M. Photoreduction at a Distance: Facile, Nonlocal Photoreduction of Ag Ions in Solution by Plasmon-Mediated Photoemitted Electrons. *Nano Lett.* **2010**, *10*, 1329–1334.
- (2) Boerigter, C.; Campana, R.; Morabito, M.; Linic, S. Evidence and implications of direct charge excitation as the dominant mechanism in plasmon-mediated photocatalysis. *Nat. Commun.* **2016**, *7*, 10545.
- (3) Mukherjee, S.; Libisch, F.; Large, N.; Neumann, O.; Brown, L. V.; Cheng, J.; Lassiter, J. B.; Carter, E. A.; Nordlander, P.; Halas, N. J. Hot Electrons Do the Impossible: Plasmon-Induced Dissociation of H₂ on Au. *Nano Lett.* **2013**, *13*, 240–247.
- (4) Schweikhard, V.; Grubisic, A.; Baker, T. A.; Thomann, I.; Nesbitt, D. J. Polarization-Dependent Scanning Photoionization Microscopy: Ultrafast Plasmon-Mediated Electron Ejection Dynamics in Single Au Nanorods. *ACS Nano* **2011**, *5*, 3724–3735.
- (5) Schweikhard, V.; Grubisic, A.; Baker, T. A.; Nesbitt, D. J. Multiphoton Scanning Photoionization Imaging Microscopy for Single-Particle Studies of Plasmonic Metal Nanostructures. *J. Phys. Chem. C* **2011**, *115*, 83–91.
- (6) Wu, K.; Chen, J.; McBride, J. R.; Lian, T. Efficient hot-electron transfer by a plasmon-induced interfacial charge-transfer transition. *Science* **2015**, *349*, 632–635.
- (7) Christopher, P.; Moskovits, M. Hot Charge Carrier Transmission from Plasmonic Nanostructures. *Annu. Rev. Phys. Chem.* **2017**, *68*, 379–398.
- (8) Park, G. B.; Krüger, B. C.; Borodin, D.; Kitsopoulos, T. N.; Wodtke, A. M. Fundamental mechanisms for molecular energy conversion and chemical reactions at surfaces. *Rep. Prog. Phys.* **2019**, *82*, 096401.
- (9) Huang, Y.; Rettner, C. T.; Auerbach, D. J.; Wodtke, A. M. Vibrational Promotion of Electron Transfer. *Science* **2000**, *290*, 111–114.
- (10) Akimov, A. V.; Prezhdo, O. V. The PYXAID Program for Non-Adiabatic Molecular Dynamics in Condensed Matter Systems. *J. Chem. Theory Comput.* **2013**, *9*, 4959–4972.
- (11) Song, H.; Fischer, S. A.; Zhang, Y.; Cramer, C. J.; Mukamel, S.; Govind, N.; Tretiak, S. First Principles Nonadiabatic Excited-State Molecular Dynamics in NWChem. *J. Chem. Theory Comput.* **2020**, *16*, 6418–6427.
- (12) Epifanovsky, E.; et al. Software for the frontiers of quantum chemistry: An overview of developments in the Q-Chem 5 package. *J. Chem. Phys.* **2021**, *155*, 084801.
- (13) Wu, Q.; Zhou, L.; Schatz, G. C.; Zhang, Y.; Guo, H. Mechanistic Insights into Photocatalyzed H₂ Dissociation on Au Clusters. *J. Am. Chem. Soc.* **2020**, *142*, 13090–13101.
- (14) Doltsinis, N. *Quantum Simulations of Complex Many-Body Systems: From Theory to Algorithms*; John von Neumann Inst. Comput., 2002; pp 377–397.
- (15) Esch, M. P.; Levine, B. G. Decoherence-corrected Ehrenfest molecular dynamics on many electronic states. *J. Chem. Phys.* **2020**, *153*, 114104.
- (16) Tully, J. C. Molecular Dynamics with Electronic Transitions. *J. Chem. Phys.* **1990**, *93*, 1061–1071.
- (17) Hammes-Schiffer, S.; Tully, J. C. Proton transfer in solution: Molecular dynamics with quantum transitions. *J. Chem. Phys.* **1994**, *101*, 4657–4667.

- (18) Jin, Z.; Subotnik, J. E. Nonadiabatic Dynamics at Metal Surfaces: Fewest Switches Surface Hopping with Electronic Relaxation. *J. Chem. Theory Comput.* **2021**, *17*, 614–626.
- (19) Dou, W.; Subotnik, J. E. A broadened classical master equation approach for nonadiabatic dynamics at metal surfaces: Beyond the weak molecule-metal coupling limit. *J. Chem. Phys.* **2016**, *144*, 024116.
- (20) Fernandez-Alberti, S.; Roitberg, A. E.; Nelson, T.; Tretiak, S. Identification of unavoided crossings in nonadiabatic photoexcited dynamics involving multiple electronic states in polyatomic conjugated molecules. *J. Chem. Phys.* **2012**, *137*, 014512.
- (21) Wang, L.; Prezhdo, O. V. A Simple Solution to the Trivial Crossing Problem in Surface Hopping. *J. Phys. Chem. Lett.* **2014**, *5*, 713–719.
- (22) Meek, G. A.; Levine, B. G. Evaluation of the Time-Derivative Coupling for Accurate Electronic State Transition Probabilities from Numerical Simulations. *J. Phys. Chem. Lett.* **2014**, *5*, 2351–2356.
- (23) Jain, A.; Alguire, E.; Subotnik, J. E. An Efficient, Augmented Surface Hopping Algorithm That Includes Decoherence for Use in Large-Scale Simulations. *J. Chem. Theory Comput.* **2016**, *12*, 5256–5268.
- (24) Granucci, G.; Persico, M.; Toniolo, A. Direct semiclassical simulation of photochemical processes with semiempirical wave functions. *J. Chem. Phys.* **2001**, *114*, 10608–10615.
- (25) Sundstrom, E. J.; Head-Gordon, M. Non-orthogonal configuration interaction for the calculation of multielectron excited states. *J. Chem. Phys.* **2014**, *140*, 114103.
- (26) Richter, M.; Marquetand, P.; González-Vázquez, J.; Sola, I.; González, L. SHARC: ab Initio Molecular Dynamics with Surface Hopping in the Adiabatic Representation Including Arbitrary Couplings. *J. Chem. Theory Comput.* **2011**, *7*, 1253–1258.
- (27) Akimov, A. V. A Simple Phase Correction Makes a Big Difference in Nonadiabatic Molecular Dynamics. *J. Phys. Chem. Lett.* **2018**, *9*, 6096–6102.
- (28) Zhou, Z.; Jin, Z.; Qiu, T.; Rappe, A. M.; Subotnik, J. E. A Robust and Unified Solution for Choosing the Phases of Adiabatic States as a Function of Geometry: Extending Parallel Transport Concepts to the Cases of Trivial and Near-Trivial Crossings. *J. Chem. Theory Comput.* **2020**, *16*, 835–846.
- (29) Ou, Q.; Fatehi, S.; Alguire, E.; Shao, Y.; Subotnik, J. E. Derivative couplings between TDDFT excited states obtained by direct differentiation in the Tamm-Dancoff approximation. *J. Chem. Phys.* **2014**, *141*, 024114.
- (30) Rom, N.; Fattal, E.; Gupta, A. K.; Carter, E. A.; Neuhauser, D. Shifted-contour auxiliary-field Monte Carlo for molecular electronic structure. *J. Chem. Phys.* **1998**, *109*, 8241–8248.
- (31) Baer, R.; Neuhauser, D. Shifted Contour Auxiliary Field Monte Carlo. *Recent Advances in Computational Chemistry*; World Scientific, 2002; Vol. 2, pp 279–310.
- (32) Plasser, F.; Ruckebauer, M.; Mai, S.; Opeľ, M.; Marquetand, P.; González, L. Efficient and Flexible Computation of Many-Electron Wave Function Overlaps. *J. Chem. Theory Comput.* **2016**, *12*, 1207–1219.
- (33) Sapunar, M.; Piteša, T.; Davidović, D.; Došlić, N. Highly Efficient Algorithms for CIS Type Excited State Wave Function Overlaps. *J. Chem. Theory Comput.* **2019**, *15*, 3461–3469.
- (34) Thorsteinsson, T.; Cooper, D. The biorthogonal method for optimizing modern valence bond wavefunctions. *Mol. Phys.* **1998**, *93*, 663–674.
- (35) Cooper, D. *Valence Bond Theory*; Elsevier, 2002. Google-Books-ID: ichMZ0Qq4VIC.
- (36) Burton, H. G. A. Generalized nonorthogonal matrix elements: Unifying Wick's theorem and the Slater-Condon rules. *J. Chem. Phys.* **2021**, *154*, 144109.
- (37) Krylov, A. I. Size-consistent wave functions for bond-breaking: the equation-of-motion spin-flip model. *Chem. Phys. Lett.* **2001**, *338*, 375–384.
- (38) Shao, Y.; Head-Gordon, M.; Krylov, A. I. The spin-flip approach within time-dependent density functional theory: Theory and applications to diradicals. *J. Chem. Phys.* **2003**, *118*, 4807–4818.
- (39) Aikens, C. M.; Li, S.; Schatz, G. C. From Discrete Electronic States to Plasmons: TDDFT Optical Absorption Properties of Ag_n ($n = 10, 20, 35, 56, 84, 120$) Tetrahedral Clusters. *J. Phys. Chem. C* **2008**, *112*, 11272–11279.
- (40) Pritchard, B. P.; Altarawy, D.; Didier, B.; Gibson, T. D.; Windus, T. L. New Basis Set Exchange: An Open, Up-to-Date Resource for the Molecular Sciences Community. *J. Chem. Inf. Model.* **2019**, *59*, 4814–4820.

Recommended by ACS

Diabatic Many-Body Expansion: Development and Application to Charge-Transfer Reactions

Amiel S. P. Paz and William J. Glover

FEBRUARY 04, 2021
JOURNAL OF CHEMICAL THEORY AND COMPUTATION

READ 

Polarizable Frozen Density Embedding with External Orthogonalization

Partha Pratim Pal, Lasse Jensen, *et al.*

OCTOBER 22, 2019
JOURNAL OF CHEMICAL THEORY AND COMPUTATION

READ 

Reduced-Scaling Approach for Configuration Interaction Singles and Time-Dependent Density Functional Theory Calculations Using Hybrid Funct...

Dávid Mester and Mihály Kállay

JANUARY 31, 2019
JOURNAL OF CHEMICAL THEORY AND COMPUTATION

READ 

Quantum Perturbation Theory Using Tensor Cores and a Deep Neural Network

Joshua Finkelstein, Anders M. N. Niklasson, *et al.*

JUNE 07, 2022
JOURNAL OF CHEMICAL THEORY AND COMPUTATION

READ 

Get More Suggestions >